Geophysical Journal International

Geophys. J. Int. (2014) doi: 10.1093/gji/ggu160

Geophysical Journal International Advance Access published May 31, 2014

3-D crustal structure of the western United States: application of Rayleigh-wave ellipticity extracted from noise cross-correlations

Fan-Chi Lin,[1] Victor C. Tsai[2] and Brandon Schmandt[3]

[1]*Department of Geology and Geophysics, The University of Utah, Salt Lake City, UT* 84112*, USA. E-mail: FanChi.Lin@utah.edu*
[2]*Seismological Laboratory, Division of Geological and Planetary Sciences, California Institute of Technology, Pasadena, CA* 91125*, USA*
[3]*Department of Earth and Planetary Science, The University of New Mexico, Albuquerque, NM* 87131*, USA*

Accepted 2014 April 29. Received 2014 April 28; in original form 2014 January 8

SUMMARY

We present a new 3-D seismic model of the western United States crust derived from a joint inversion of Rayleigh-wave phase velocity and ellipticity measurements using periods from 8 to 100 s. Improved constraints on upper-crustal structure result from use of short-period Rayleigh-wave ellipticity, or Rayleigh-wave H/V (horizontal to vertical) amplitude ratios, measurements determined using multicomponent ambient noise cross-correlations. To retain the amplitude ratio information between vertical and horizontal components, for each station, we perform daily noise pre-processing (temporal normalization and spectrum whitening) simultaneously for all three components. For each station pair, amplitude measurements between cross-correlations of different components (radial–radial, radial–vertical, vertical–radial and vertical–vertical) are then used to determine the Rayleigh-wave H/V ratios at the two station locations. We use all EarthScope/USArray Tranportable Array data available between 2007 January and 2011 June to determine the Rayleigh-wave H/V ratios and their uncertainties at all station locations and construct new Rayleigh-wave H/V ratio maps in the western United States between periods of 8 and 24 s. Combined with previous longer period earthquake Rayleigh-wave H/V ratio measurements and Rayleigh-wave phase velocity measurements from both ambient noise and earthquakes, we invert for a new 3-D crustal and upper-mantle model in the western United States. Correlation between the inverted model and known geological features at all depths suggests good resolution in five crustal layers. Use of short-period Rayleigh-wave H/V ratio measurements based on noise cross-correlation enables resolution of distinct near surface features such as the Columbia River Basalt flows, which overlie a thick sedimentary basin.

Key words: Interferometry; Surface waves and free oscillations; Seismic tomography; Wave propagation; Crustal structure; North America.

1 INTRODUCTION

Ambient noise cross-correlations are widely used to study shallow Earth structure (e.g. Yao *et al.* 2008; Moschetti *et al.* 2010a). In most applications, long duration vertical component noise time series recorded at two stations are first cross-correlated to approximate the Rayleigh-wave Green's function between the two station locations (e.g. Sabra *et al.* 2005; Shapiro *et al.* 2005; Bensen *et al.* 2007). Phase and group velocity dispersion measurements are then measured for each cross-correlation and surface wave traveltime tomography is performed (Yao *et al.* 2006; Lin *et al.* 2007, 2008). The depth range that can be resolved by ambient noise tomography is often controlled by the observed spectrum of the Rayleigh wave signals, where for most regional and continental scale studies the signals are strongest near the primary (∼16 s) and secondary microseism periods (∼8 s) and the structure is best resolved roughly between 5 and 30 km depth (Ritzwoller *et al.* 2011). To resolve shallower crustal structure, small-scale dense seismic arrays are often needed to extract shorter period surface waves (Yang *et al.* 2011; Lin *et al.* 2013a; Mordret *et al.* 2013). Some applications utilizing body waves extracted from noise cross-correlations to study deep Earth structure are also starting to emerge (Poli *et al.* 2012; Boué *et al.* 2013; Lin & Tsai 2013; Lin *et al.* 2013b; Nishida 2013). There has also been growing interest in extracting useful surface wave amplitude information using ambient noise cross-correlation (Lawrence & Prieto 2011; Lin *et al.* 2011a; Prieto *et al.* 2011; Tsai 2011; Weaver 2011, 2013; Zhang & Yang 2013).

Recently, we showed that intermediate to long-period (24–100 s) teleseismic Rayleigh-wave ellipticity, or Rayleigh-wave H/V (horizontal to vertical amplitude) ratio can be jointly inverted with Rayleigh-wave phase velocity measurements to better resolve crustal structure (Lin *et al.* 2012a). Similar to local surface wave

phase and group velocities (Lin *et al.* 2009; Pollitz & Snoke 2010; Lin & Ritzwoller 2011), in a laterally smoothly varying medium, the Rayleigh-wave H/V ratio is a frequency dependent property controlled solely by the 1-D structure beneath the seismometer (Tanimoto & Rivera 2008; Yano *et al.* 2009). Including Rayleigh-wave H/V ratio measurements from 24 to 100 s in inversions for crustal structure allowed resolution not only of *Vs* in the uppermost 3 km but also density and *Vp*/*Vs* ratios in the uppermost 3 km layer (Lin *et al.* 2012a).

The method presented here differs significantly from traditional analysis of the H/V ratio of raw noise spectra at seismographs (Nakamura 1989; Fäh *et al.* 2001; Sánchez-Sesma *et al.* 2011). Interpretation of the H/V ratio of raw noise spectra depends on the assumed noise character (i.e. whether it is dominantly Rayleigh waves, dominantly body waves or a mixture between various different wave types; see Bonnefoy-Claudet *et al.* 2006 for a review). In contrast, the relationship between the Rayleigh-wave H/V ratio measurement and 1-D seismic structure is well defined (Tanimoto & Rivera 2008). In this paper, we sometime refer to the Rayleigh-wave H/V ratio as 'the H/V ratio' for conciseness and the term should not be confused with the traditional noise spectral H/V ratio.

Shorter period H/V ratio measurements based on ambient noise cross-correlations rather than longer period earthquake Rayleigh waves are desirable because they are strongly sensitive to near-surface structure. Recently, based on noise data collected by a temporary small-scale regional array in Canterbury, New Zealand, Savage *et al.* (2013) demonstrated that the amplitudes of different component ambient noise cross-correlations can be extremely sensitive to sediment thickness near the basement resonance frequency. In that study, strong 1st higher mode Rayleigh waves were observed between 1 and 2.5 s period in the radial–radial cross-correlations but were mostly absent in the vertical–vertical cross-correlations implying an extremely high 1st higher mode Rayleigh-wave H/V ratio. Their observation was found to be consistent with synthetic seismograms accounting for very low velocities related to ∼1.5-km-thick sediments in the area.

Here we show that with careful noise pre-processing it is possible to obtain robust short-period Rayleigh-wave H/V amplitude ratio measurements by using multicomponent ambient noise cross-correlations. We use all available data between 2007 January and 2001 June from EarthScope/USArray Transportable Array (TA; Fig. 1) to demonstrate the new method. We then combine the short-period H/V ratio measurements made in this study with previous intermediate- to long-period H/V ratio measurements (Lin *et al.* 2012a) and short- to long-period phase velocity measurements (Lin *et al.* 2008; Lin *et al.* 2009; Lin & Ritzwoller 2011) to invert for a new crustal and upper-mantle model of the western United States. We show that, with the short-period H/V ratio measurements from ambient noise cross-correlations, we can now resolve structure in the uppermost 1 km and consequently mitigate trade-offs between near-surface and deeper crustal parameters in tomographic models of the western United States.

2 DATA PROCESSING TO PRODUCE THE MULTI-COMPONENT RAYLEIGH-WAVE GREEN'S FUNCTIONS

In this study, we slightly modify the method described by Bensen *et al.* (2007) to pre-process the three-component (LHZ, LHE and LHN) daily noise records of USArray before cross-correlation to ensure the amplitude ratios between vertical and horizontal components are not altered. For each station and each component, we first remove the mean, trend and instrument response from the daily noise time series. We then apply a 15–60 s bandpass filter to extract the most energetic surface wave signals. A 128-s-time window running absolute mean (Bensen *et al.* 2007) is applied to the 15–60 s bandpassed signals to calculate the temporal normalization function. For each station and each time, we divide all the unfiltered three component noise records simultaneously by the maximum of the temporal normalization functions from the three components to suppress earthquake signals. After temporal normalization, we then perform spectral whitening by dividing the spectrum of each component by the average of the three-component smoothed spectrum.

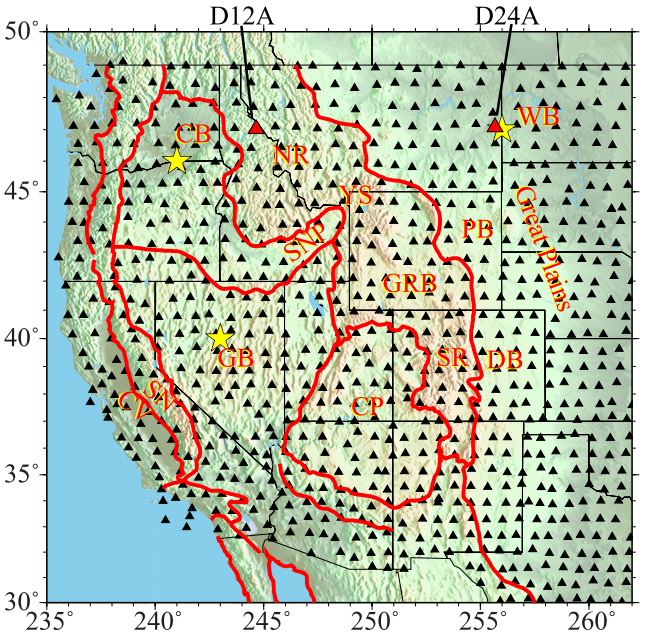

Figure 1. The USArray Transportable Array (TA) stations used in this study are identified by black triangles. The two red triangles mark the two stations, D12A and D24A, used in Figs 2 and 3. The three stars identify locations used in Figs 9 and 10. Red lines mark the tectonic boundaries in the western United States. Several major geological features mentioned in the text are also shown (WB: Williston Basin; PB: Powder River Basin; GR: Green River Basin; DB: Denver Basin; NR: Northern Rockies; SR: Southern Rockies; CP: Colorado Plateau; SNP: Snake River Plain; CB: Columbia Basin; GB: Great Basin; SN: Sierra Nevada; CV: Central Valley; YS: Yellowstone).

For each station pair, we closely follow the method described by Lin *et al.* (2008). First, we calculate the nine component cross-correlations between vertical (Z) and two horizontal (N and E) components. We then rotate the cross-correlations involving horizontal components into radial (R) and transverse (T) directions through a rotation matrix (e.g. Lin *et al.* 2008). To improve the signal-to-noise ratio (SNR), we sum the positive and negative components of each cross-correlation to obtain the symmetric component cross-correlation. Fig. 2(a) shows an example of the ZZ, ZR, RZ and RR symmetric component cross-correlations between two TA stations D12A (Avery, Idaho) and D24A (Glendive, Montana) bandpassed near 16 s period. Clear Rayleigh wave signals are observed on all four components. While the arrival times are approximately the same for all four components, the observed amplitudes, which are determined based on the maximum of the envelope functions, are very different.

Assuming a diffusive noise wavefield (Lobkis & Weaver 2001; Snieder 2004), the negative time derivative of the ZZ, ZR, RZ and

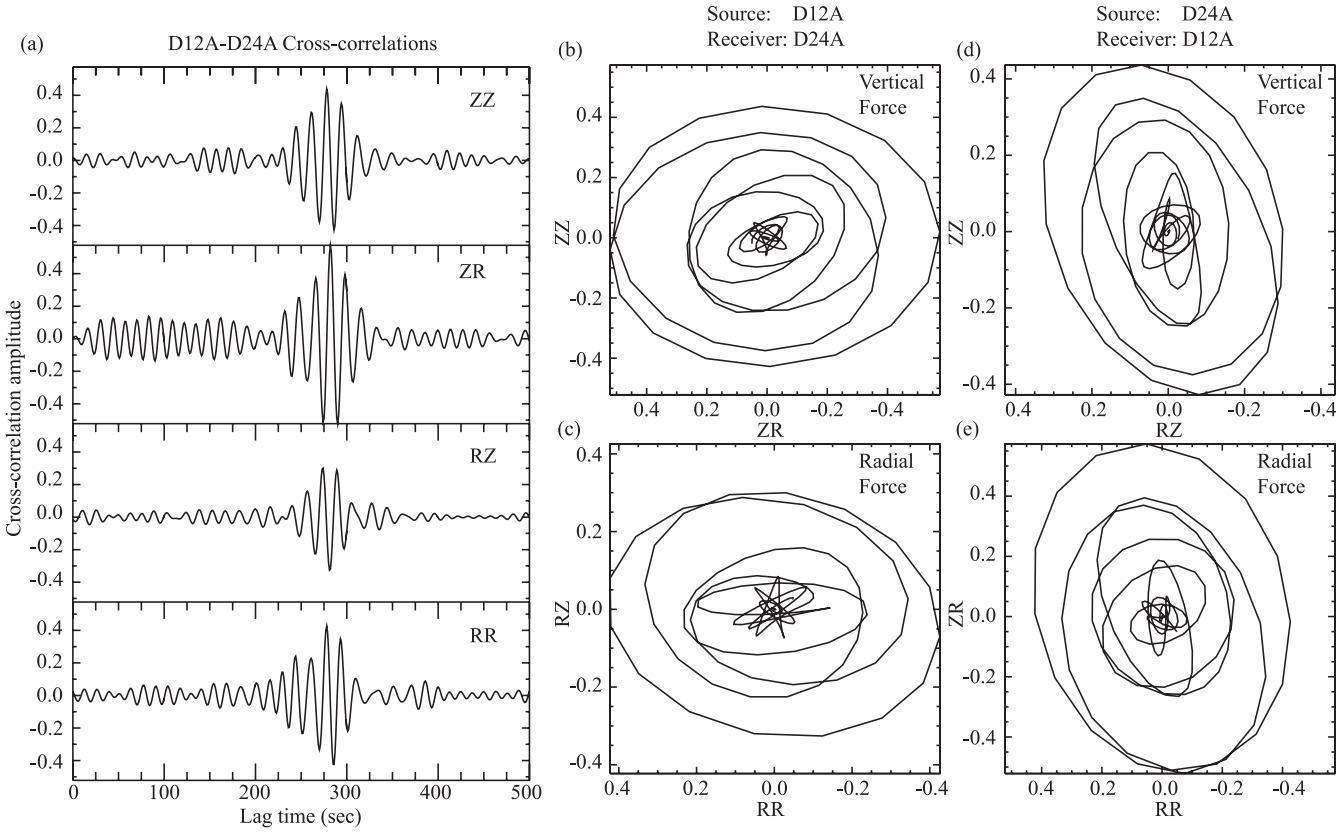

Figure 2. (a) Four component (ZZ, ZR, RZ and RR) symmetric ambient noise cross-correlations between stations D12A and D24A bandpassed near 16 s period. Clear Rayleigh wave signals are observed on all four components. (b) The 16-s Rayleigh-wave particle motion in radial and vertical directions observed at the receiver station D24A excited by a vertical force at the virtual source D12A. (c) Same as (b) but for a horizontal force. (d)–(e) Same as (b)–(c) but with D12A being the receiver and D24A being the virtual source.

RR cross-correlations can be related to the Rayleigh-wave Green's functions for a point force in the vertical (Z) and radial (R) direction at the first station and observed on either the vertical (Z) and radial (R) direction at the second station (the first letter represents the force direction at the first station and the second letter represents the receiver direction at the second station). The combination of ZZ and ZR cross-correlations (Fig. 2b) or RZ and RR cross-correlations (Fig. 2c) hence allows us to study the Rayleigh-wave particle motion at the second station (receiver) excited by either a vertical or radial force, respectively, at the first station (virtual source). Based on the reciprocity of the Green's functions, we can also consider the second station as the virtual source and the first station being the receiver. In this case, the combination of ZZ and RZ cross-correlations (Fig. 2d) or ZR and RR cross-correlations (Fig. 2e) allows us to study the Rayleigh-wave particle motion at the first station excited by either a vertical or radial force, respectively, at the second station location. While the ambient noise wavefield is likely not perfectly diffusive, when the station distance satisfies the far field condition, the Rayleigh wave particle motion constructed here is expected to be similar to those excited by a ballistic source. This can be shown for a semi-diffusive wavefield using the stationary phase approximation (Snieder 2004). Conceptually, this can be understood as the same noise signals contributing to the Rayleigh wave observed in different component cross-correlations are dominantly coming from the directions aligned with the two stations. These noise signals can be considered excited by small ballistic sources and our normalization and cross-correlation processes do not change the amplitude ratio information between different components. Caution must be taken, however, when far field criterion is not satisfied or the noise wavefield is not semi-diffusive, where, like phase velocity, H/V ratio measurements can be biased.

For the D12A–D24A cross-correlations, the ∼16 s Rayleigh-wave particle motions observed at each receiver location from the two different force directions are mostly consistent, and clear differences are observed for the particle motions at the two sites. For D24A (Figs 2b and c), which is located on top of the Williston Basin (Gerhard *et al.* 1982), the amplitude in the radial component is clearly larger than the vertical component, resulting in a high horizontal (H) over vertical (V) amplitude ratio. D12A (Figs 2d and e), on the other hand, is located in the Northern Rockies in an area with crystalline rock near the surface, and the Rayleigh-wave particle motion is elongated in the vertical direction and hence has a low H/V ratio. Due to the strong sensitivity of the H/V ratio to shallow crustal structure, the different H/V ratios observed at these two sites likely reflects the difference in shallow structure where these two stations are located.

3 RAYLEIGH-WAVE H/V RATIO MEASUREMENTS AND MAPS

To determine the H/V ratio at a station location for each period, all available virtual sources are used, where for each virtual source station we average the two H/V ratio measurements based on the vertical and radial force. We impose several selection criteria to retain only the most reliable measurements. First, similar to our phase velocity measurements (Lin *et al.* 2008), we remove all

virtual source stations that are within three wavelengths of the target stations (assuming 4 km s^{-1} phase velocity) to satisfy the far-field approximation. Second, we remove all virtual source stations with Rayleigh-wave SNR smaller than 8 on any of the four components (ZZ, ZR, RZ or RR). Third, we remove all virtual source stations with an inconsistent Rayleigh-wave phase traveltime observed in the ZR, RZ or RR cross-correlation compared to the traditional phase traveltime measurement based on the ZZ component cross-correlation. Here we define any traveltime difference larger than one-fourth of a period as inconsistent. Note that because of the retrograde particle motion of Rayleigh waves, waves excited by a radial force are expected to have phase arrivals one-fourth of a period later than those excited by a vertical force. Similarly, waves observed on the radial component are expected to arrive one-fourth of a period earlier than those observed in the vertical component. We take these predicted phase shifts into account when checking for traveltime consistency. Fourth, we remove all virtual source stations with H/V ratio measurement differences between the vertical and radial force larger than 10 per cent. The combination of the third and fourth criteria ensures the consistency of measurements from different component noise cross-correlations since the measured H/V ratio is only meaningful if the different component observations represent the same Rayleigh wave propagating between the two stations. The total number of measurements removed by each selection criteria is period dependent. At 16 s, the number of measurements removed by the distance, SNR, traveltime consistency and amplitude ratio consistency selection criteria are roughly 3, 23, 5 and 34 per cent of the total 890 944 initial H/V ratio measurements between all available virtual sources and receivers (1215 TA stations).

Fig. 3 shows the distribution of H/V ratio measurements satisfying the above selection criteria for receiver station D12A and D24A at 16 s period using more than 270 virtual source stations. Clear differences again can be observed between the H/V ratio measurements at the two receiver stations, where mostly high H/V ratios (>1.0) are observed for station D24A and mostly low H/V ratios (<1.0) are observed for station D12A. For each station, we use the mean and the standard deviation of the mean of the H/V ratio measurement distribution to determine the best estimated H/V ratio and its uncertainty at the station location assuming that all measurements are independent and measurement errors are Gaussian. While the variability on each individual H/V ratio measurement (the standard deviation) is large, the uncertainty of the mean (the standard deviation of the mean) is significantly smaller due the large number of measurements. However, the uncertainty is likely somewhat underestimated here because part of the measurement variability is not due to random Gaussian errors but due to systematic biases. For example, the presence of azimuthal anisotropy can cause directionally dependent H/V measurements, which are not accounted for in our uncertainty estimation. Determining azimuthal anisotropy using H/V ratio measurements is beyond the scope of this study, and will be the subject of future work.

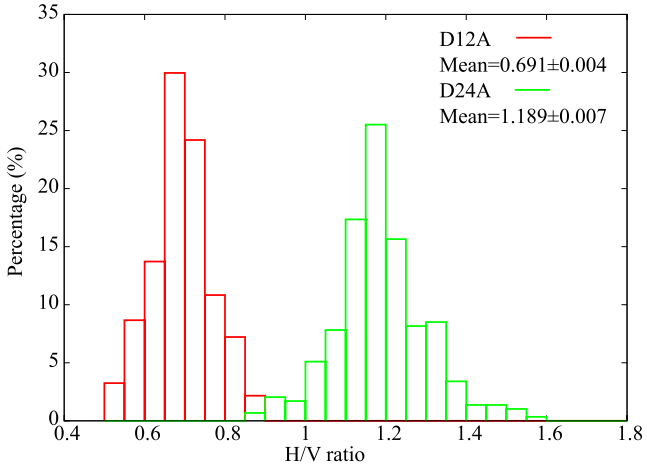

Figure 3. The distribution of 16-s Rayleigh-wave H/V ratio measurements at D12A (red) and D24A (green) using all available virtual sources across USArray stations. The mean and the standard deviation of the mean of the distributions are also shown, which are used to determine the H/V ratios and their uncertainties at the two station locations.

The existence of ∼70 km station spacing of USArray in the western United States allows us to interpolate the H/V ratio measurements and determine Rayleigh-wave H/V ratio maps with a resolution compatible with surface wave phase velocity tomography maps (e.g. Lin *et al.* 2009; Lin & Ritzwoller 2011). Similar resolution of the phase velocity and H/V ratio maps facilitates a joint inversion, which we describe later in the text. To obtain the H/V ratio and uncertainty maps, we interpolate the results at all station locations onto a $0.2^\circ \times 0.2^\circ$ grid by applying 0.5° Gaussian smoothing. For each location, the smoothed H/V ratio is typically constrained by H/V ratios observed at the three to four nearest stations. This not only allows us to retain the desired ∼70 km resolution but also suppresses irregular stations with inconsistent H/V ratios. Irregular H/V ratios are likely due to localized small-scale anomalies, if not persistent instrument biases, that cannot be resolved in our phase velocity maps. Before the interpolation, we remove all stations with fewer than 50 measurements from different virtual sources or if the estimated uncertainty is larger than 20 per cent of the estimated H/V ratio to retain only the receiver stations with robust H/V ratio measurements.

Fig. 4 summarizes the best-estimated H/V ratios and their uncertainties across all the TA stations in the western United States at 8 and 16 s periods. At periods of 8 and 16 s (Figs 4a and b), high H/V ratio areas are clearly correlated with major sedimentary basins in the western United States (e.g. the Williston Basin and the Denver Basin; see Fig. 1). Within the centre of the Williston Basin, extremely high H/V ratios (>3) are observed at 8 s, likely due to the large shear velocity contrast between the shallow sediments and deeper Precambrian bedrock. Additionally, this period may be close to the resonance frequency of the sedimentary basin (Savage *et al.* 2013). Unlike Rayleigh wave phase velocity measurements, which are mostly positively sensitive to deeper *Vs* structure, H/V ratio measurements are most sensitive to *Vs* structure near the surface and the sensitivity changes sign from negative to positive going from shallow to deep (Fig. 5). While low H/V ratios observed at 16 s are mostly correlated with major mountain ranges in the western United States (e.g. the Northern Rockies and Southern Rockies), the lowest H/V ratio (<0.7) observed at 8 s is located within the Columbia Basin (Fig. 4a). At 8 s, the H/V ratio is negatively sensitive to *Vs* structure shallower than ∼2 km depth but positively sensitive to *Vs* structure between ∼2 and 10 km depth. In this area, a ∼3-km-thick layer of basalt (Miocene Columbia River flood basalt) overlies a 5–8-km-thick sedimentary basin (Saltus 1993). The unusual combination of high velocity near the surface and lower velocity just beneath (Catchings & Mooney 1988) is the likely reason for the minimal H/V ratio observed here.

The uncertainties of the H/V measurements at 8 and 16 s are generally smaller than 1 per cent of the estimated value and are higher near the western edge of our map where small-scale wave front distortion might be important due to the large lateral velocity

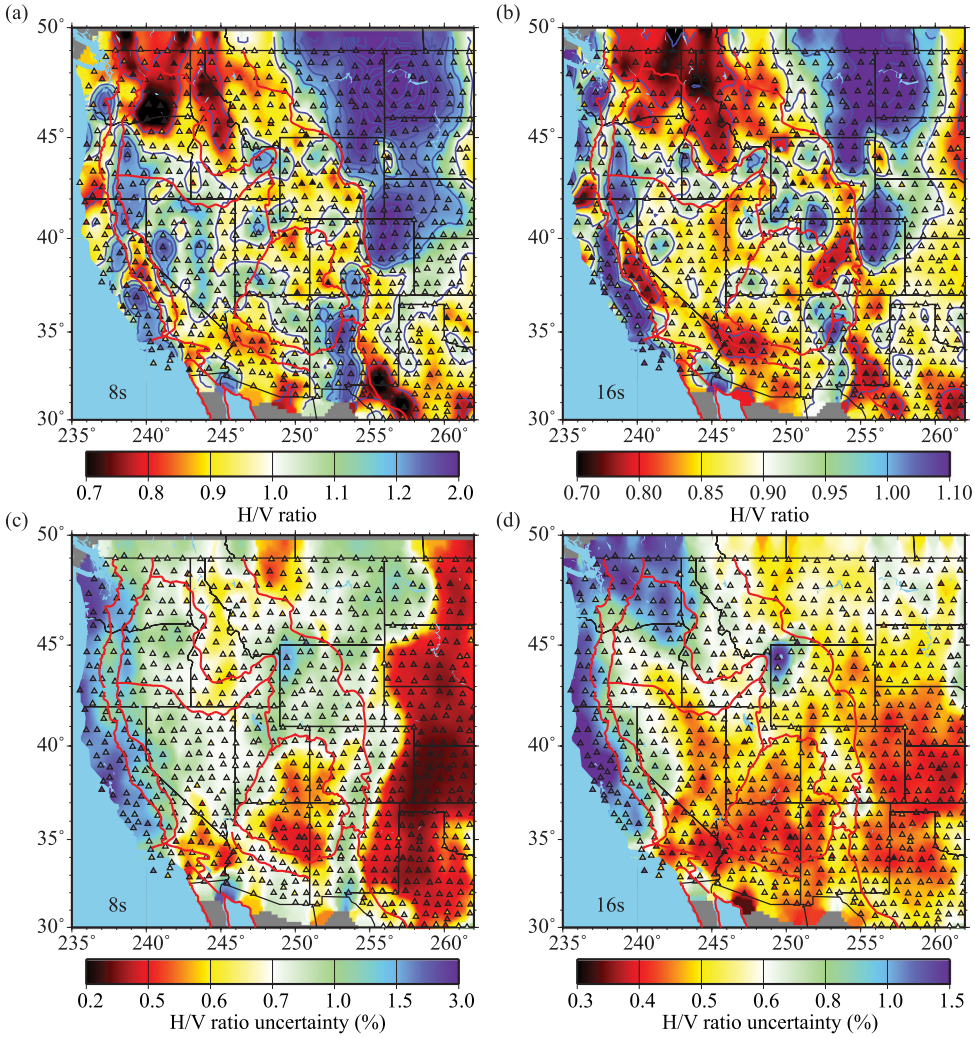

Figure 4. (a)–(b) 8- and 16-s Rayleigh-wave H/V ratios observed across USArray. A Gaussian smoothing method is used to interpolate H/V ratios at all station locations onto a grid, which results in the H/V ratio map. Contours are separated by intervals of 0.2 in (a) and 0.1 in (b). (c)–(d) The H/V ratio uncertainties for (a)–(b).

variations near the active plate boundary. Similar higher uncertainty near the western edge was also observed in Rayleigh wave phase velocity measurements based on ambient noise cross-correlations and eikonal tomography (Lin *et al.* 2009). Higher uncertainty is also observed near Yellowstone, likely related to the abrupt structure change due to the existence of an extremely low velocity magma chamber (Chu *et al.* 2010). Lower uncertainty is observed within the Great Plains where less lateral velocity variation is expected.

Similar to ambient noise phase and group velocity measurements, H/V ratio measurements are most robust between 8 and 24 s period where the microseism energy is strong. While longer period (>30 s) velocity measurements have been shown to be possible based on vertical–vertical ambient noise cross-correlations (e.g. Bensen *et al.* 2008), the SNR of Rayleigh wave signals decreases quickly in the radial component noise cross-correlations above 20-s period likely due to the stronger incoherence of noise recorded in the horizontal components (Fig. 6a; Lin *et al.* 2008). Our selection criterion that requires SNR > 8 for ambient noise Rayleigh waves causes the total number of acceptable H/V ratio measurements to decrease rapidly above 20 s (Fig. 6b). Consequently, we do not use H/V ratio information from ambient noise for periods longer than 24 s.

At a period of 24 s, we can compare the H/V ratios measured in this study based on ambient noise cross-correlations to the results of a previous study based on teleseismic Rayleigh waves (Fig. 7; Lin *et al.* 2012a). In general, the observed H/V ratios are consistent between the two types of measurements. Similar to the results at 16 s (Fig. 4b), high H/V ratios are observed in major sedimentary basin (e.g. the Williston and Denver Basins) and low H/V ratios are observed in major mountain ranges (e.g. the Northern and Southern Rockies). Notice that for ∼30 per cent of TA locations there are no valid 24 s H/V ratio results based on ambient noise cross-correlations. This is mainly due to the poor SNR in the radial component cross-correlations and hence insufficient number of measurements (<50) at those locations. The lower SNR and hence the smaller number of measurements for each station is also reflected in higher estimated uncertainties at 24 s (Fig. 7c) compared to the results for shorter periods (Figs 4c and d).

Figs 8(a) and (b) show the differences of the observed H/V ratios between ambient noise and earthquake measurements at 24 s across the TA stations and Fig. 8(c) shows the distribution of the differences. At a majority of the locations (∼75 per cent of the covered area) the differences are less than 4 per cent, but differences

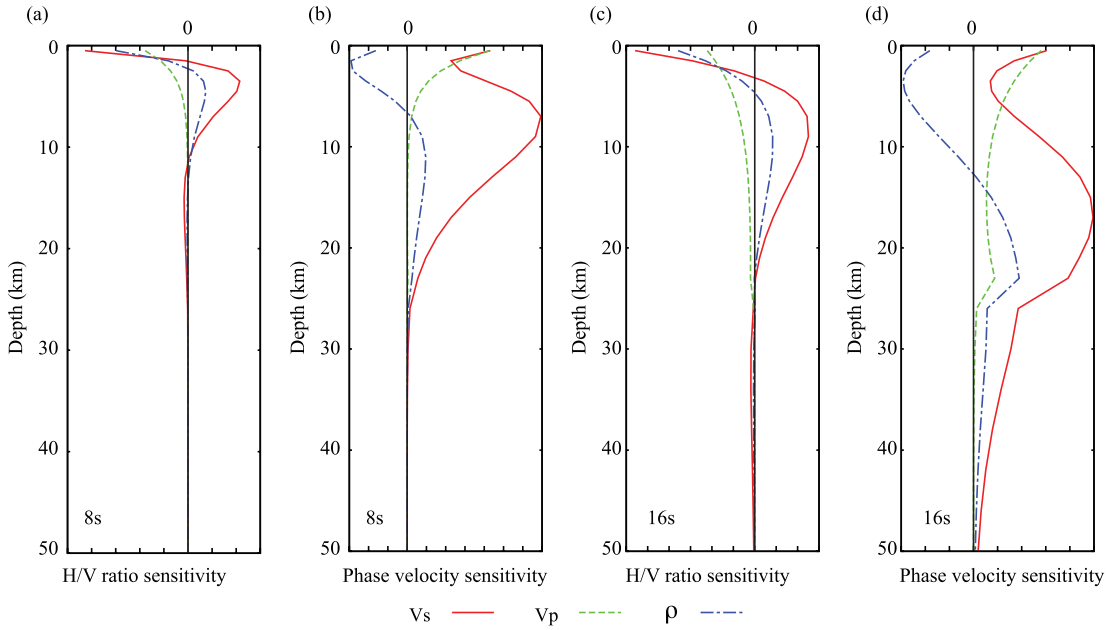

Figure 5. (a)–(b) The 8-s Rayleigh-wave H/V ratio and phase velocity depth sensitivity kernels related to *Vs* (red solid line), *Vp* (green dashed line) and density (blue dashed line) calculated based on the 1-D PREM model without the ocean layer (Dziewonski & Anderson 1981). (c)–(d) Same as (a)–(b) but for 16-s Rayleigh waves.

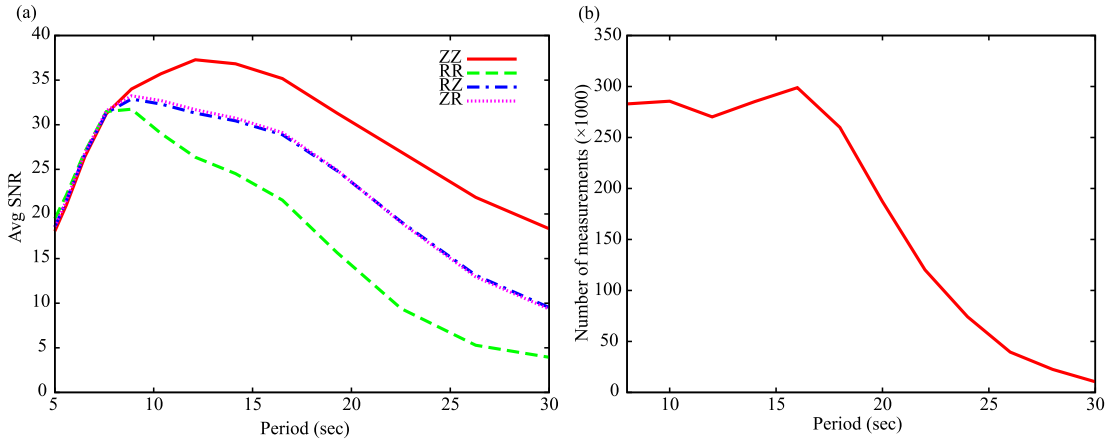

Figure 6. (a) Average signal-to-noise ratio (SNR) for Rayleigh waves observed for the four component (ZZ, ZR, RZ and RR) ambient noise cross-correlations shown as a function of period. (b) Total number of H/V ratio measurements in the western United States in this study satisfying our selection criteria. The number of measurements drops significantly above ∼20 s period due to the overall low SNR in the RR cross-correlations.

larger than 5 per cent are observed mainly near the western edge of the map. This, again, is likely due to the strong lateral velocity variations in this area. Also, because the TA is truncated at the coastline, there are no virtual sources on the western side of stations near the coast for ambient noise H/V ratio measurements, but for teleseismic earthquake measurements Rayleigh waves arrive from almost all back-azimuths. Measurements from different back-azimuths can vary systematically due to effects including multipathing, regional small-scale 3-D structure perturbation and azimuthal anisotropy, which are not accounted for in our analysis. Based on the difference distribution (Fig. 8c), no clear systematic bias is observed between the H/V ratio measurements from the two different source types. However, the variability of the differences suggests that the uncertainties are slightly underestimated. If we exclude the apparent outliers with measurement differences larger than 6 per cent, which are mostly measurements near the coast and likely suffered from systematic biases, the standard deviation of the difference is ∼2.5 per cent. This can be compared to the estimated ∼1.5 per cent averaged rms of ambient noise and earthquake measurement uncertainties (Figs 7c, d and 8d). Here, similar to our phase velocity measurements (Lin *et al.* 2009), we multiply the uncertainties by a factor of 1.5 to provide a more realistic estimate.

4 JOINT INVERSION OF RAYLEIGH-WAVE PHASE VELOCITY AND H/V RATIO

The ability to extract reliable short-period Rayleigh-wave H/V ratios from noise cross-correlations allows us to combine them with previous broad-band Rayleigh-wave phase velocity measurements (Lin *et al.* 2008; Lin *et al.* 2009; Lin & Ritzwoller 2011) and longer period H/V ratio measurements (Lin *et al.* 2012a) to perform a broad-band 3-D inversion. Fig. 9 shows examples of the observed Rayleigh-wave phase velocities and H/V ratios at three locations in

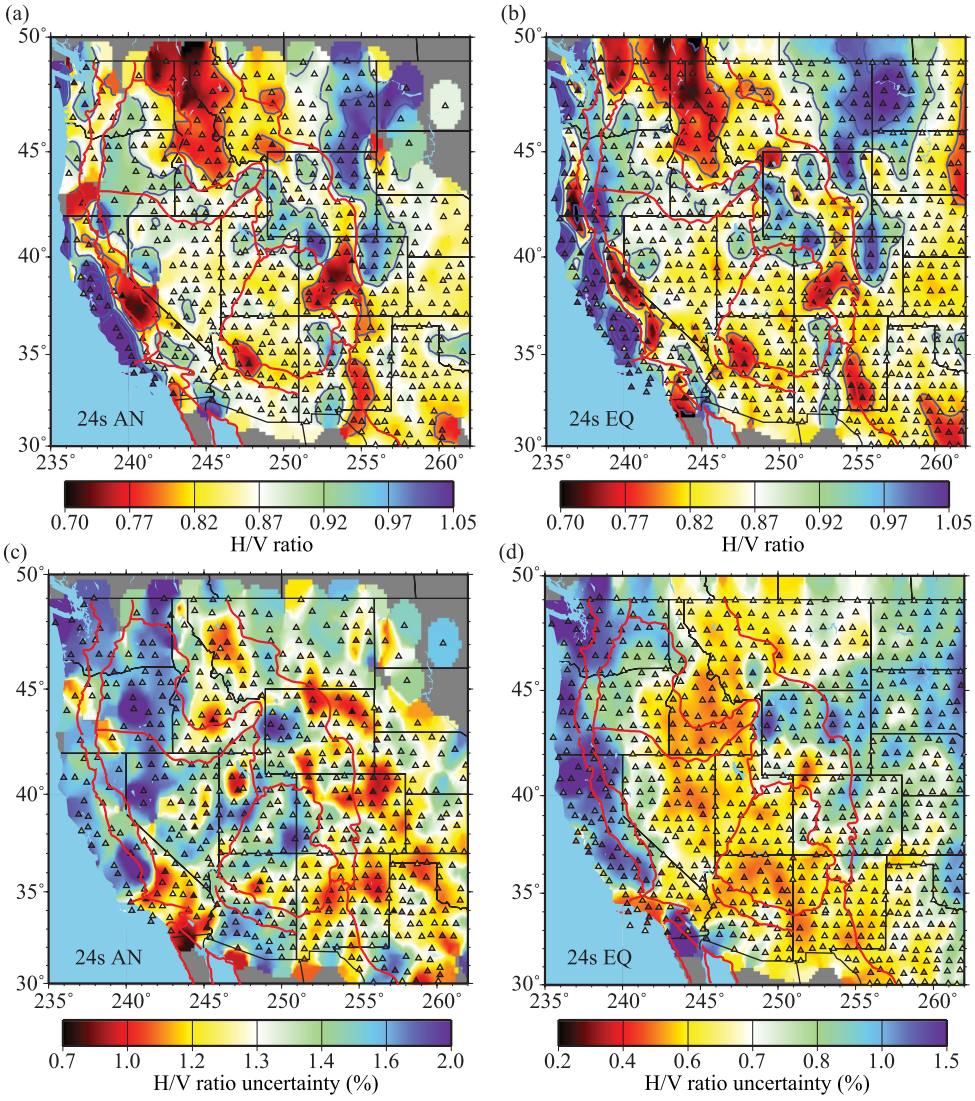

Figure 7. (a) Same as Fig. 4(b) but for 24-s Rayleigh waves. Stations with less than 50 measurements are removed from our analysis, which results in several station gaps in the map. (b) Same as (a) but based on teleseismic Rayleigh-wave H/V ratio measurements made in Lin *et al.* (2012a). (c)–(d) The H/V ratio uncertainties for (a)–(b). Notice that the colour scales are different in (c) and (d), where uncertainties are overall higher for ambient noise measurements at 24 s.

the western United States. Phase velocity dispersion curves all have a common pattern with a steeper slope at short periods and a more gradual slope at long periods due to the sensitivity transition from crust to mantle and broadening of the depth range of sensitivity. In contrast, there is much more variation between the H/V ratio as a function of frequency at different locations due to shallower sensitivity and large variations in upper-crustal properties.

For each location, similar to Lin *et al.* (2012a), we jointly invert Rayleigh-wave phase velocity and H/V ratio measurements between 8 and 100 s for a 1-D *Vs* model in the crust and upper mantle and a *Vp*/*Vs* ratio and density model in the upper crust (Fig. 10). In this study, the crustal model contains five layers with the first three upper-crustal layers being 1, 2 and 8 km thick. Compared to Lin *et al.* (2012a), an additional uppermost 1 km layer is used because of the new short period H/V ratio measurements. The middle and lower crustal layers are set to have equal thicknesses, which are locally determined using previously estimated Moho depths based on receiver functions (Gilbert 2012). We parameterize the mantle model from the Moho to 250 km depth with five cubic B-splines. A two-step steepest descent inversion is used to minimize the overall χ^2 misfit, where in the first step we only perturb *Vs* parameters and keep both *Vp*/*Vs* and density parameters fixed to their initial reference values (Table 1). In the second step, the model from step one is used as the initial reference model but, in additional to all *Vs* parameters, the *Vp*/*Vs* ratio and density in the three upper-crustal layers are also allowed to change. In step two, weak damping is applied such that *Vp*/*Vs* ratio and density are only perturbed at those locations that have a high misfit. Throughout the inversion, we iteratively update the depth sensitivity kernels of our measurements to account for non-linearity of the inversion and we also require that *Vs* increase with depth monotonically. To demonstrate that the top 1 km structure is indeed resolvable with our new observation, we also perform a test inversion with only four crustal layers by replacing the top two 1- and 2-km-thick crustal layers with a single 3-km-thick top crustal layer (Figs 9 and 10d–f). A summary of the model parameters used in our inversion is shown in Table 1.

The predicted frequency-dependent Rayleigh-wave phase velocity and H/V ratio based on the inverted five crustal layer 1-D models

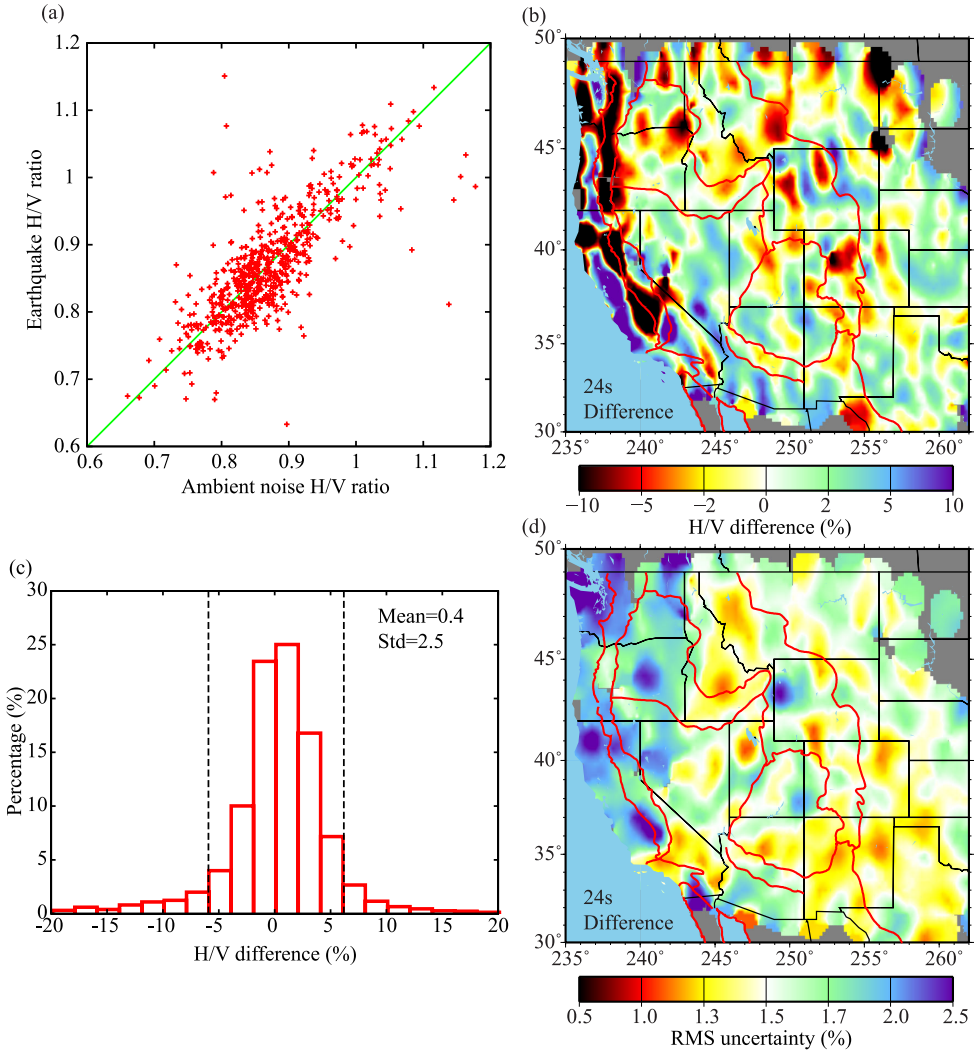

Figure 8. (a) Scatterplot of ambient noise and earthquake 24-s H/V ratio measurements for USArray stations. (b) The percentage difference between Figs 7(a) and (b) (subtract 7b from 7a). (c) The distribution of the percentage differences shown in (b). The mean and standard deviation of the distribution for differences smaller than 6 per cent (within dashed lines) are also shown. (d) The expected uncertainty of (b) calculated based on the root-mean-square of Figs 7(c) and (d).

(Figs 10a–c) generally agree well with the observed measurements (Fig. 9). At a point in the Great Basin (243°, 40°), the observed H/V ratio has a distinct local minimum and a local maximum at around 20 and 50 s period, respectively (Fig. 9b). The inversion shows that relatively low *Vs* in the middle crustal layer (3.43 km s^{-1} compared to 3.69 and 3.82 km s^{-1} at the two other locations) is required to fit the observations (Fig. 10a). This is consistent with the low *Vs* and strong radial anisotropy ($V_{SV} < V_{SH}$) middle/lower crust detected in this region by previous studies (Moschetti *et al.* 2010a,b). We have no sensitivity to resolve radial anisotropy in this study, as we only analyze Rayleigh waves. The test inversion with four crustal layers cannot explain the observed short-period H/V ratio measurements (Fig. 9b) and the χ^2 misfit is significantly higher.

At a point within the Columbia Basin (241°, 46°), extremely low H/V ratios are observed at short periods (<0.7 at 8 s; Fig. 9d) and an H/V ratio maximum is observed near 40 s period. The five crustal layer 1-D inversion at this location shows that a relatively fast 0–1 km layer (2.75 km s^{-1} compared to 1.40 and 0.70 km s^{-1} at the two other locations) and a relatively slow 3–11 km layer (2.84 km s^{-1} compared to 3.40 and 3.52 km s^{-1} at the two other locations) are needed to fit the phase velocity and H/V ratio measurements. This is consistent with the fast Columbia River Basalt layer sitting on top of a thick sedimentary basin in this area (Saltus 1993). Noteworthy is that traditional ambient noise tomography based on traveltime measurements can detect the thick sedimentary basin in this area (e.g. Moschetti *et al.* 2010a), but does not have the sensitivity to resolve the high velocity basalt structure near the surface. Resolution of the uppermost 1 km is only possible due to inclusion of the short-period H/V ratio measurements used in this study. At this location, the four and five crustal layer inversions perform equally well since the top two crustal layers in the five crustal layer inversion have the same *Vs* (Fig. 10a). The exact same *Vs* in the first two crustal layers is due to the monotonic constraint imposed and allowing velocity reversal could potentially further improve the overall misfit.

At a point within the Williston Basin (256°, 47°), the most striking feature in the observed H/V ratio is its approximately exponential increase with decreasing period below about 30 s (Fig. 9f). The shortest period, 8 s, is likely close to the resonance period of the basin structure here, resulting in an H/V ratio larger than 3. The inversion result shows that extremely low *Vs* upper crust in the top 3 km (particularly in the top 1 km) is needed to fit the observations, confirming the expected structure of the sedimentary basin

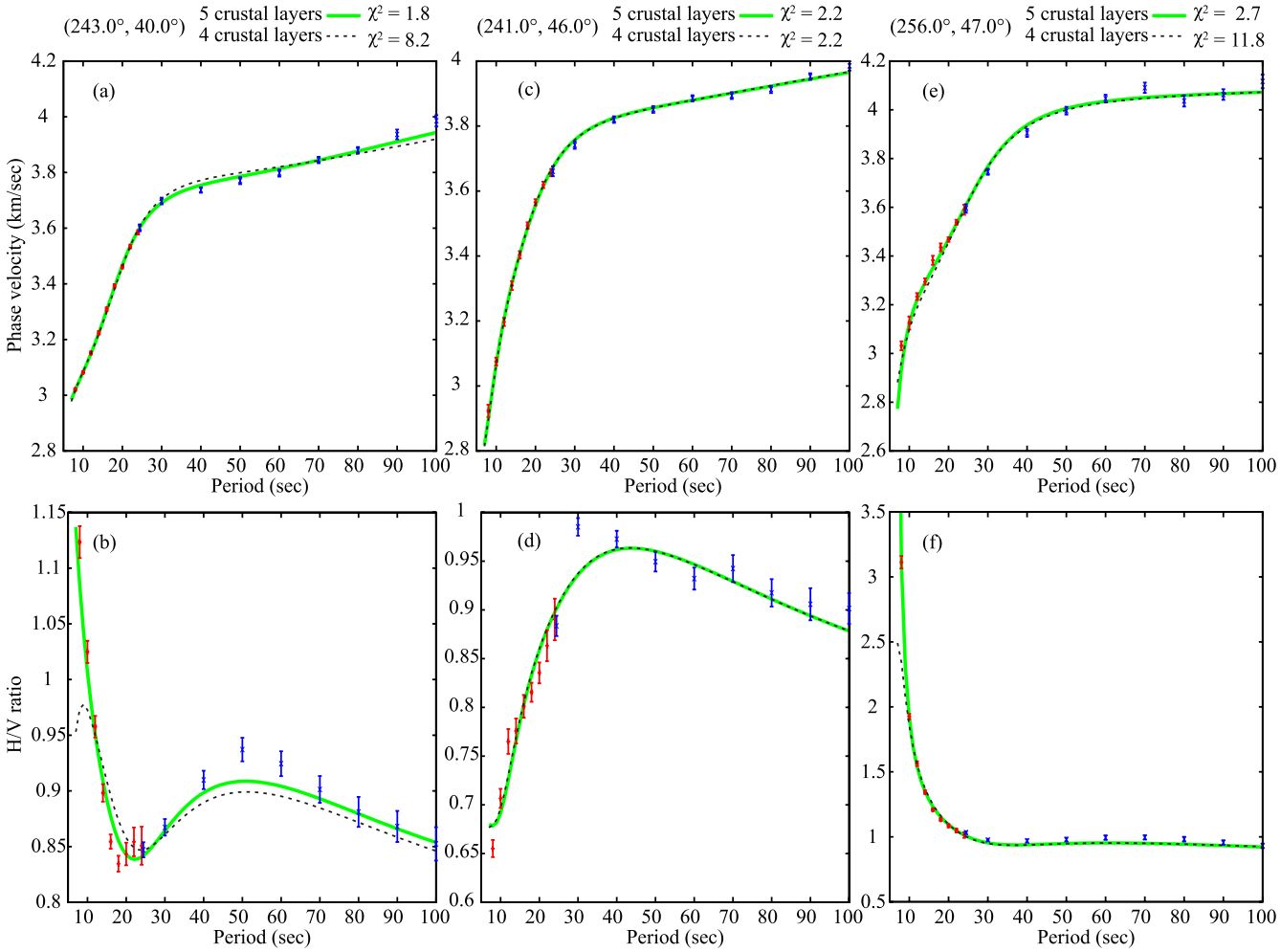

Figure 9. (a) The observed Rayleigh-wave phase velocity dispersion at location (243°, 40°) within the Great Basin (star in Nevada in Fig. 1). Red and blue bars represent the phase velocities and their uncertainties for ambient noise and earthquake measurements, respectively. The green solid and black dashed lines are the predicted phase velocity dispersion curve based on the inverted 1-D models with five crustal layers shown in Figs 10(a)–(c) and four crustal layers shown in Figs 10(d)–(f), respectively. (b) Same as (a) but for H/V ratio measurements. (c)–(d) Same as (a)–(b) but for location (241.0°, 46.0°) near the Columbia Basin (star near the Washington/Oregon border in Fig. 1). (e)–(f) Same as (a)–(b) but for location (256.0°, 47.0°) near the Williston Basin (star near the Montana/North Dakota border in Fig. 1).

(Gerhard *et al.* 1982). At this point, different from at the other two example locations, perturbations of upper-crustal density and *Vp*/*Vs* ratio parameters are required to obtain an acceptable fit to the phase velocity dispersion and H/V ratio measurements. The χ^2 misfit reduces from 6.72 in the first step of the inversion, where only *Vs* parameters are allowed to change, to 2.65 in the second step of the inversion, where upper-crustal *Vp*/*Vs* ratio and density parameters are also allowed to change. The low density and high *Vp*/*Vs* ratio in the upper crust are consistent with the shallow sedimentary structure here (Brocher 2005) and also in agreement with our previous study (Lin *et al.* 2012a). The test inversion based on the four crustal layer model cannot explain the H/V ratio greater than 3 observed at 8 s period (Fig. 9f).

The fact that the test inversion with four crustal layers cannot fully explain our short period H/V ratio observation (e.g. Figs 9b and f), whereas the preferred five crustal layer inversion does explain these data, clearly demonstrates the resolvability of the top 1 km crustal structure with the new measurements presented here. While the 8 s H/V ratio is sensitive to both the top 1 km structure and slightly deeper structure down to 10 km (Fig. 5a), the deeper structure is already constrained by phase velocity and longer H/V ratio measurements. This allows the short period H/V ratio measurements to provide unique constraints to the uppermost crustal structure without trading off with deeper structure. Overall, the inverted structure deeper than 11 km is very similar between the test and preferred inversions but substantial differences are observed in the upper-crustal layers (Fig. 10). In the following section, we focus our discussion on our preferred five crustal layer model.

5 THE INVERTED 3-D MODEL

We combine all the inverted 1-D models across the western United States to produce the final 3-D model. Figs 11(a)–(e) show the *Vs* model for each of the five crustal layers and Fig. 11(f) shows the mantle *Vs* model at 80 km depth. In general, our mantle model is very similar to previous studies (e.g. Lin *et al.* 2012a) as short period H/V ratio measurements mostly add new constraints on crustal structure (Fig. 5). The uncertainty of our inverted model is higher near the Pacific coast and Yellowstone where small-scale structural variations are present and the measurement uncertainties are higher

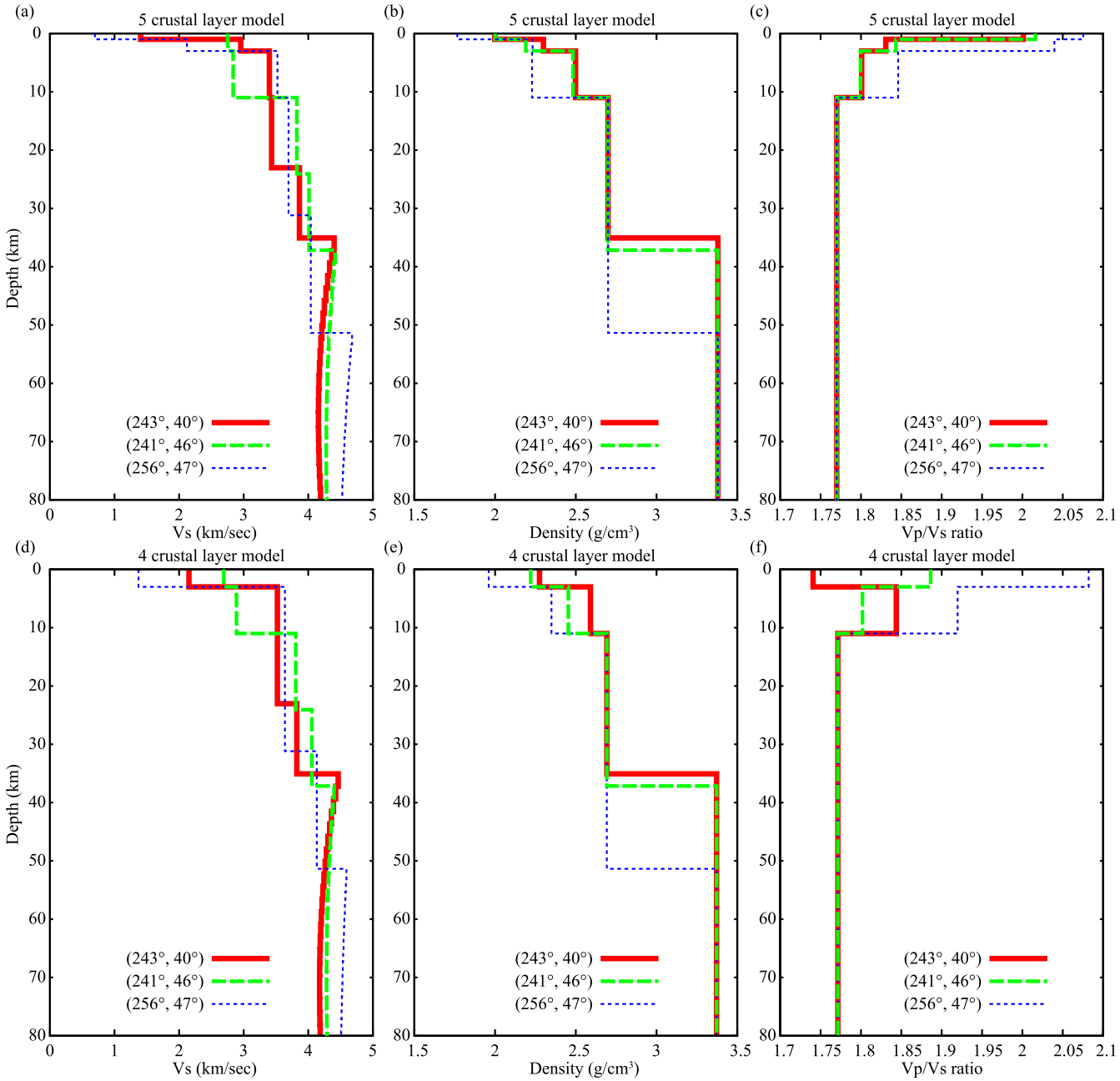

Figure 10. (a) The inverted 1-D *Vs* models with five crustal layers for the dispersion curves shown in Fig. 9 (243°, 40°: solid red; 241°, 46°: dashed green; 256°, 47°: dotted blue). (b)–(c) Same as (a) but for 1-D density and *Vp*/*Vs* ratio models. (d)–(f) Same as (a)–(c) but for the test inversion with four crustal layers.

(Figs 4c, d and 7c, d; Lin *et al.* 2009). Caution should be used when interpreting the model in those regions.

In the top 1-km-crustal layer, clear correlation is observed between the *Vs* model and near-surface geological features (Fig. 11a). Note that we do not account for topography in our 1-D inversions and the zero depth has a different elevation for different locations. Low *Vs* anomalies are mostly observed within major sedimentary basins and alluvial plains in the western United States (e.g. Williston Basin, Denver Basins and Great Plains). At several locations, *Vs* is lower than 0.7 km s^{-1}, likely due to shallow unconsolidated sediments. High *Vs* anomalies, on the other hand, are mostly correlated with crystalline outcrops in mountain ranges, and also flood basalts in the Columbia Basin. A relatively high *Vs* anomaly is observed at the Black Hills, which is a basement-cored uplift of the Laramide orogeny that is surrounded by sedimentary basins near the border of Wyoming and South Dakota (Tikoff & Maxson 2001). This feature nicely illustrates the ∼70 km lateral resolution of the 3-D model, which is controlled by the USArray station spacing.

While many of the features observed in the second crustal layer (1–3 km depth; Fig. 11b) are similar to those in the shallowest layer, there are also notable differences. For example, clear low *Vs* anomalies are now only observed in the centre of deep sedimentary basins. Adjacent to deep sedimentary basins (e.g. the Williston Basin, Powder River Basin and Denver Basin), high *Vs* anomalies observed in the Great Plains likely reflect relatively high *Vs* bedrock beneath a near-surface sediment layer. High *Vs* anomalies are also

Table 1. Model parameters.

Crustal layer	Thickness (km)	*Vs* (km s^{-1})	Density (g cm^{-3})	*Vp/Vs* ratio
Upper crust 1	3	2.5 (0.3–4.2)	2.3 (0.5–3.5)	1.83 (1.7–5.0)
Upper crust 2	8	2.7 (1.5–4.2)	2.5 (1.8–3.5)	1.8 (1.7–2.3)
Upper crust 1	1	2.0 (0.3–4.2)	2.0 (0.5–3.5)	2.0 (1.7–5.0)
Upper crust 2	2	2.5 (1.5–4.2)	2.3 (1.5–3.5)	1.83 (1.7–2.5)
Upper crust 3	8	2.7 (1.5–4.2)	2.5 (1.8–3.5)	1.8 (1.7–2.3)
Middle crust	(Moho-11)/2	3.2 (1.5–4.2)	2.7	1.77
Lower crust	(Moho-11)/2	3.2 (1.5–4.2)	2.7	1.77
Mantle 5 B-splines	–	4.3 (3.5–5)	3.38	1.77

Notes: The red, blue, and black text denote reference model parameters used in the four crustal layer test inversion, five crustal layer inversion, and both inversions, respectively. Moho depth is taken from a recent receiver function study (Gilbert 2012). The *Vs*, density, and *Vp/Vs* parameters correspond to the reference model and the perturbation ranges are shown within parentheses.

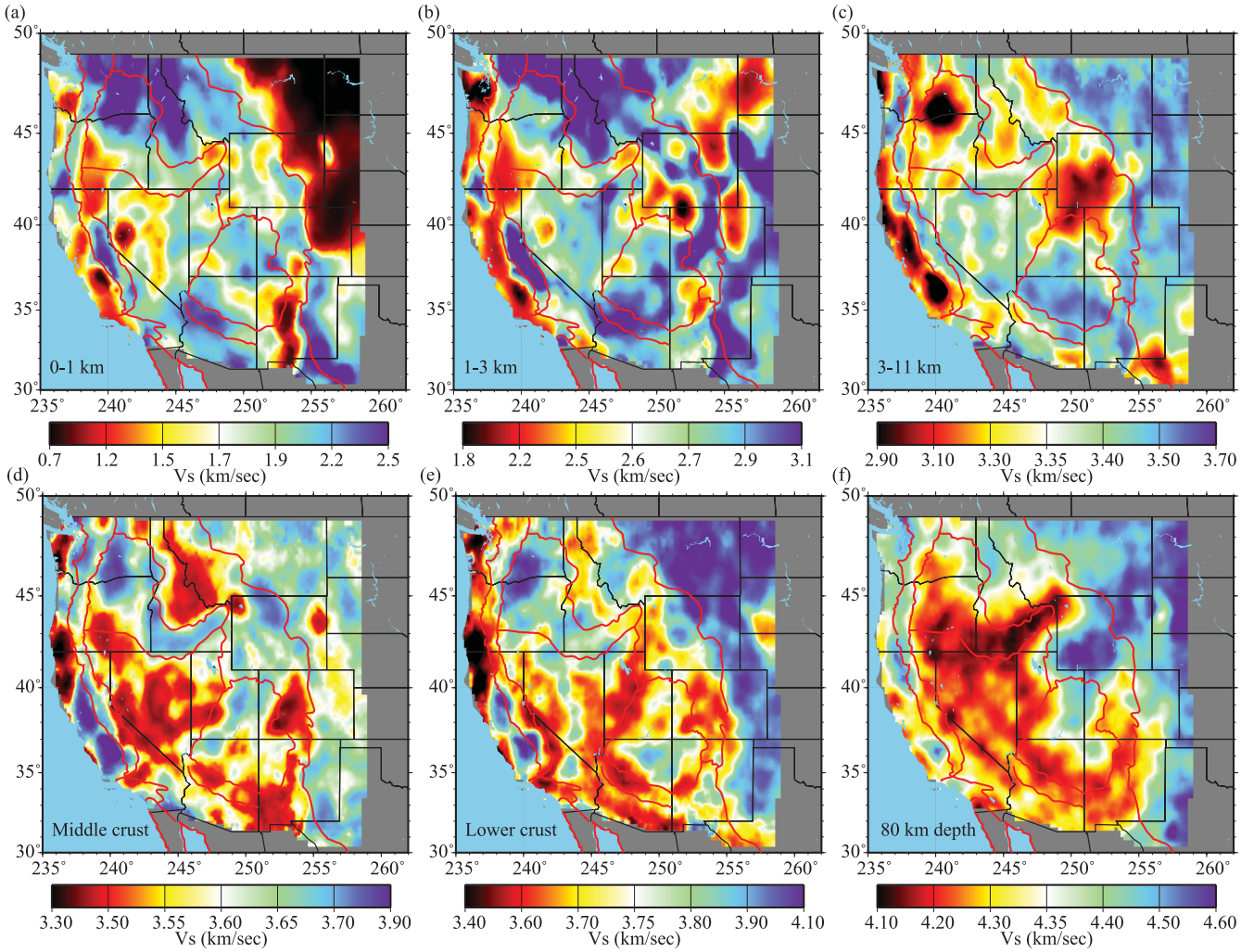

Figure 11. The inverted 3-D *Vs* model at different depths: (a) 0–1 km, (b) 1–3 km, (c) 3–11 km, (d) middle crust, (e) lower crust and (f) 80 km depth.

observed within major mountain ranges such as the Northern and Southern Rockies. In contrast to the second upper-crustal layer, the most apparent features in the third crustal layer (3–11 km depth; Fig. 11c) are the low *Vs* anomalies of Green River Basin, Columbia Basin and Central Valley, which represent the deepest basins in the western United States that are greater than 70 km across. The large velocity anomaly contrast in the Columbia Basin between the first and third upper-crustal layers demonstrates the outstanding vertical resolution near the surface due to the inclusion of short period H/V ratio measurements.

In the middle crustal layer (Fig. 11d), major low *Vs* anomalies are observed near the Mendocino Triple Junction and within the Basin and Range, Southern Rockies and Northern Rockies. The area of slow middle crust in the Great Basin is similar to the area where strong crustal anisotropy is also observed and may be related to extensional deformation (Moschetti *et al.* 2010b; Lin *et al.* 2011b).

However, low *Vs* middle crust beneath the Southern Rockies and Northern Rockies spans areas that experienced modest Cenozoic extension compared to the Great Basin (Christiansen & Yeats 1992). Post-Laramide intraplate magmatism, which is common to all these provinces (Walker *et al.* 2004, www.navdat.org) with low *Vs* middle crust, is probably more closely related to the isotropic *Vs* structure than the magnitude of post-Laramide crustal extension.

Localized high *Vs* anomalies in the middle crust are observed beneath the Central Valley, Columbia Basin and Snake River Plain. Relatively subtle high *Vs* anomalies in the middle crust are broadly distributed beneath the Great Plains and the Wyoming craton. Near the western plate margin, high *Vs* anomalies in the middle crust likely reflect mafic compositions related to accreted oceanic crust beneath the Central Valley (Godfrey *et al.* 1997) and Oregon coast (Trehu *et al.* 1994). Beneath the Columbia Basin the high *Vs* may also be related to mafic composition owing to a combination of accretion of oceanic crust and backarc rifting following Eocene initiation of the Cascadia subduction zone (Catchings & Mooney 1988; Gao *et al.* 2011; Schmandt & Humphreys 2011).

Anomalous *Vs* structure in the lower crustal layer (Fig. 11e) is vertically continuous with middle crustal structure in some locations, but the *Vs* images of the lower and middle crust structure are distinct across large areas of the western United States. Low *Vs* extends from the middle to lower crustal layers near the Mendocino Triple Junction and southern Oregon coast. However, in the western United States interior anomalously low *Vs* in the lower crust is observed near the edges of the Colorado Plateau and Great Basin, which differs from the pattern observed in the middle crustal layer. The lower crustal distribution of low *Vs* is similar to the distribution of Quaternary volcanism in the Basin and Range and Southern Rockies (Walker *et al.* 2004), and may reflect recent or ongoing intrusion of melts into the lower crust. The most laterally extensive high *Vs* anomaly in the lower crust underlies the elevated and tectonically quiescent western Great Plains. More localized high *Vs* anomalies that are vertically continuous with middle crustal anomalies are found near the western plate margin beneath the Central Valley and Columbia Basin. The ability to resolve different geological features within different crustal layers (Figs 11a–e) suggests the number of crustal layers in the inversion is appropriate for the vertical resolution of the Rayleigh wave dispersion and H/V ratio measurements.

In addition to isotropic *Vs* structure, we also investigate the density and *Vp*/*Vs* ratio structure needed in the upper crust to fit our observed Rayleigh-wave phase velocity and H/V ratio dispersion curves (Lin *et al.* 2012a). The inverted density and *Vp*/*Vs* ratio in the top two layers are summarized in Fig. 12. In general, the observed density and *Vp*/*Vs* ratio structure in the top two upper-crustal layers is consistent with prior imaging using only longer period H/V

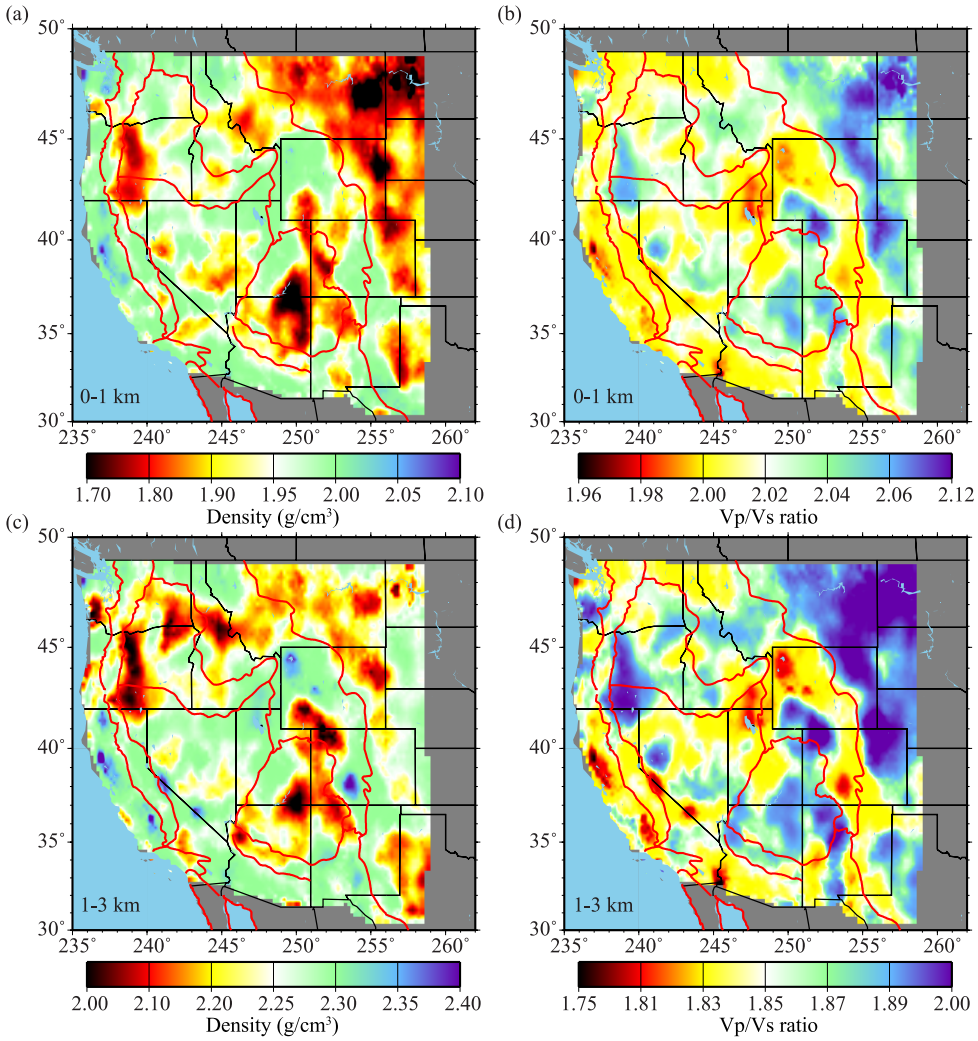

Figure 12. (a)–(b) The inverted density and *Vp*/*Vs* ratio model in the uppermost crustal layer. (c)–(d) Same as (a)–(b) but for the 1–3 km upper-crustal layer.

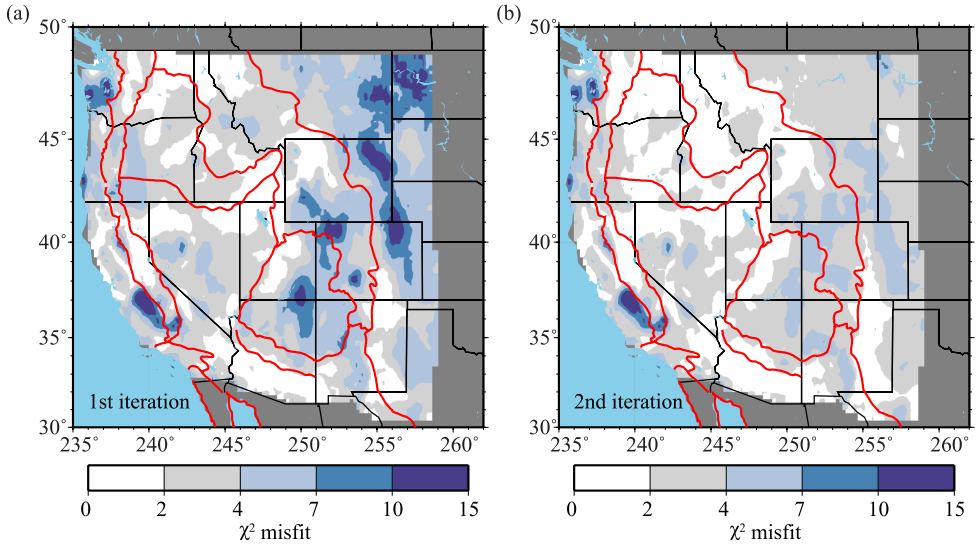

Figure 13. (a)–(b) The summary of χ^2 misfits for our two step inversions.

ratio measurements (Lin *et al.* 2012a). Low density and high *Vp*/*Vs* ratio are mostly correlated with slow anomalies in the upper crust and major sedimentary basins such as the Williston Basin, Powder River Basin, Denver Basin and Green River Basin. In these areas, our first step inversion without density and *Vp*/*Vs* ratio perturbations results in unacceptably large χ^2 misfits (i.e. $\chi^2 > 4$; Fig. 13a), but the χ^2 misfits are significantly improved in our second inversion (Fig. 13b) when both density and *Vp*/*Vs* ratio are allowed to vary. The only location where the χ^2 misfit remains high after the second inversion is in central California near the boundary between the Central Valley and Sierra Nevada. At this location, some stations in the valley do not have sufficiently good short-period H/V ratio measurements and the presence of a sharp structural contrast nearby introduces incompatible results during our map interpolation.

The density and *Vp*/*Vs* ratio are mostly unperturbed for those regions with low misfits in our first step inversion due to the damping regularization applied. Because our model's reference density in the top 3 km is slightly lower than normal crystalline rock density (Brocher 2005), our top 3 km density model may be slightly low for those regions without thick sedimentary rock near the surface. As described in Lin *et al.* (2012a), there are tradeoffs between *Vs*, density and *Vp*/*Vs* ratio and the damping regularization stabilizes our second step inversion. There are also tradeoffs between density and *Vp*/*Vs* ratio in different upper-crustal layers, which results in very similar patterns in the observed density and *Vp*/*Vs* structure shown in Fig. 12. We also investigated whether deeper density and *Vp*/*Vs* ratio are needed to further improve the χ^2 misfit, particularly in the Great Plains, Green River Basin and Colorado Plateau. Additional constraints, such as receiver functions (Shen *et al.* 2013a,b) and surface wave amplification (Lin *et al.* 2012b), however, are needed to mitigate trade-offs between the different parameters at greater depths.

6 CONCLUDING REMARKS

In this study, we show that robust short period Rayleigh-wave H/V ratio measurements can be extracted from multicomponent ambient noise cross-correlations with careful pre-processing to consistently normalize multicomponent noise records. To ensure that the amplitude ratios between the vertical and horizontal components stay intact, we apply both temporal normalization and spectrum whitening simultaneously for the three-component daily noise records for each station. All available USArray stations in the western United States operating between 2007 January and 2011 June (more than 1200 stations) are used both as virtual sources as well as receivers. All valid measurements are then used to statistically estimate both the H/V ratios at all station locations and their uncertainties. The consistency between ambient noise and earthquake based 24-s Rayleigh-wave H/V ratio measurements demonstrate that the H/V ratio extracted from ambient noise is likely not biased by the seismic interferometry method.

The ability to measure short-period H/V ratios, combined with previous studies (Lin *et al.* 2008, 2009, 2012a; Lin & Ritzwoller 2011), now allows 3-D inversions to be done in the western United States with broad-band (8–100 s) phase velocity and H/V ratio dispersion measurements. Our inversion suggests that models with five crustal layers and five mantle B-splines can fit both types of measurements within an acceptable level of misfit. In particular, the inclusion of short period H/V ratios provides constraints necessary to resolve distinct structures in the uppermost ∼1 km of the crust and also allows deeper crustal features to be better resolved by reducing tradeoffs with strongly heterogeneous near-surface structure. Distinct geological features are observed at different depths in our new model of the western United States crust. For example, in the Columbia Basin, a high velocity uppermost crust, slow lower upper crust and fast middle and lower crust are observed, which is in agreement with prior active source imaging and gravity inversions in the area (Catchings & Mooney 1988; Saltus 1993).

The ability to resolve better 3-D crustal structure with inversions using multiple types of seismic data can lead to better understanding of crustal composition. By jointly inverting for two independent datasets, we show that not only *Vs* but also density and *Vp*/*Vs* ratio can be constrained with surface-wave measurements. Recently, Shen *et al.* (2013a,b) demonstrated that joint inversion of receiver functions and surface-wave dispersion measurements from the TA improved the resolution of crustal and upper-mantle imaging in the western United States. A joint inversion of surface wave dispersion, H/V ratio measurements and receiver functions will be a natural extension of this study.

ACKNOWLEDGEMENTS

The data used in this research were obtained from the IRIS Data Management Center and originate predominantly from the Transportable Array component of USArray. The authors are grateful to the editor Yehuda Ben-Zion, Vedran Lekic and an anonymous reviewer for comments that helped improve this paper. This research was supported by a grant from the U.S. National Science Foundation, grant EAR-1252191.

REFERENCES

Bensen, G.D., Ritzwoller, M.H., Barmin, M.P., Levshin, A.L., Lin, F., Moschetti, M.P., Shapiro, N.M. & Yang, Y., 2007. Processing seismic ambient noise data to obtain reliable broad-band surface wave dispersion measurements, *Geophys. J. Int.,* **169,** 1239–1260.

Bensen, G.D., Ritzwoller, M.H. & Shapiro, N.M., 2008. Broad-band ambient noise surface wave tomography across the United Stated, *J. geophys. Res.,* **113,** B05306, doi:10.1029/2007JB005248.

Bonnefoy-Claudet, S., Cotton, F. & Bard, P.-Y., 2006. The nature of the seismic noise wave field and its implication for site effects studies: a literature review, *Earth Sci. Rev.,* **79**(3–4), 205–227.

Boué, P., Poli, P., Campillo, M., Pedersen, H., Briand, X. & Roux, P., 2013. Teleseismic correlations of ambient seismic noise for deep global imaging of the Earth, *Geophys. J. Int.,* **194**(2), 844–848.

Brocher, T., 2005. Empirical relations between elastic wavespeeds and density in the Earth's crust, *Bull. seism. Soc. Am.,* **95**(6), 2081–2092.

Catchings, R.D. & Mooney, W.D., 1988. Crustal structure of the Columbia Plateau: evidence for continental rifting, *J. geophys. Res.,* **93**(B1), 459–474.

Christiansen, R.L. & Yeats, R.S., 1992. Post-Laramide geology of the Cordilleran region, in *The Cordilleran orogen: Conterminous U.S.: Boulder,* Vol. G-3, pp. 261–406, eds Burchfiel, B.C., Lipman, P.W. & Zoback, M.L.C., Geological Society of America, Geology of North America.

Chu, R., Helmberger, D.V., Sun, D., Jackson, J.M. & Zhu, L., 2010. Mushy magma beneath Yellowstone, *Geophys. Res. Lett.,* **37,** L01306, doi:10.1029/2009GL041656.

Dziewonski, A.M. & Anderson, D.L., 1981. Preliminary reference Earth model, *Phys. Earth planet. Inter.,* **25,** 297–356.

Fäh, D., Kind, F. & Giardini, D., 2001. A theoretical investigation of average *H/V* ratios, *Geophys. J. Int*., **145,** 535–549.

Gao, H., Humphreys, E.D., Yao, H. & van der Hilst, R.D., 2011. Crust and lithosphere structure of the northwestern US with ambient noise tomography: Terrane accretion and Cascade arc development, *Earth planet. Sci. Lett.,* **304,** 202–211.

Gerhard, L.C., Anderson, S.B., LeFever, J.A. & Carlson, C.G., 1982. Geological development, origin, and energy mineral resources of Williston Basin, North Dakota, *AAPG Bull.,* **66,** 989–1020.

Gilbert, H., 2012. Crustal structure and signatures of recent tectonism as influenced by ancient terranes in the western United States, *Geosphere,* **8,** 141–157.

Godfrey, N.J., Beaudoin, B.C. & Klemperer, S.L. Mendocino working group, 1997. Ophiolitic basement to the Great Valley forearc basin, California, from seismic and gravity data: implications for crustal growth at the North American continental margin, *Geol. Soc. Am. Bull.,* **109,** 1536–1562.

Lawrence, J.F. & Prieto, G.A., 2011. Attenuation tomography of the western United States from ambient seismic noise, *J. geophys. Res.,* **116,** B06302, doi:10.1029/2010JB007836.

Lin, F. & Ritzwoller, M.H., 2011. Helmholtz surface wave tomography for isotropic and azimuthally anisotropic structure, *Geophys. J. Int.,* **186,** 1104–1120.

Lin, F., Ritzwoller, M.H. & Snieder, R., 2009. Eikonal tomography: surface wave tomography by phase front tracking across a regional broad-band seismic array, *Geophys. J. Int.,* **177**(3), 1091–1110.

Lin, F.C., Ritzwoller, M.H., Townend, J., Savage, M. & Bannister, S., 2007, Ambient noise Rayleigh wave tomography of New Zealand, *Geophys. J. Int.,* **170,** 649–666.

Lin, F.C., Moschetti, M.P. & Ritzwoller, M.H., 2008. Surface wave tomography of the western United States from ambient seismic noise: Rayleigh and Love wave phase velocity maps, *Geophys. J. Int.,* **173,** 281–298.

Lin, F.C., Ritzwoller, M.H. & Shen, W., 2011a. On the reliability of attenuation measurements from ambient noise cross-correlations, *Geophys. Res. Lett.,* **38,** L11303, doi:10.1029/2011GL047366.

Lin, F., Ritzwoller, M.H., Yang, Y., Moschetti, M.P. & Fouch, M.J., 2011b. Complex and variable crustal and uppermost mantle seismic anisotropy in the western United States, *Nat. Geosci.,* **4,** 55–61.

Lin, F.C., Schmandt, B. & Tsai, V.C., 2012a. Joint inversion of Rayleigh wave phase velocity and ellipticity using USArray: constraining velocity and density structure in the upper crust, *Geophys. Res. Lett.,* **39,** L12303, doi:10.1029/2012GL052196.

Lin, F.C., Tsai, V.C. & Ritzwoller, M.H., 2012b. The local amplification of surface waves: a new observable to constrain elastic velocities, density, and anelastic attenuation, *J. geophys. Res.,* **117,** B06302, doi:10.1029/2012JB009208.

Lin, F.C., Li, D., Clayton, R.W. & Hollis, D., 2013a. High-resolution 3D shallow crustal structure in Long Beach, California: Application of ambient noise tomography on a dense seismic array, *Geophysics,* **78**(4), Q45–Q56.

Lin, F.C., Tsai, V.C., Schmandt, B., Duputel, Z. & Zhan, Z., 2013b. Extracting seismic core phases with array interferometry, *Geophys. Res. Lett.,* **40**(6), 1049–1053.

Lin, F.C. & Tsai, V.C., 2013. Seismic Interferometry with Antipodal Station Pairs, *Geophys. Res. Lett.,* **40,** doi:10.1002/grl.50907.

Lobkis, O.I. & Weaver, R.L., 2001. On the emergence of the Green's function in the correlations of a diffuse field, *J. acoust. Soc. Am.,* **110,** 3011–3017.

Mordret, A., Shapiro, N.M., Singh, S., Roux, P. & Barkved, O.I., 2013. Helmholtz tomography of ambient noise surface wave data to estimate Scholte wave phase velocity at Valhall Life of the Field, *Geophysics,* **78**(2), WA99–WA109.

Moschetti, M.P., Ritzwoller, M.H., Lin, F.C. & Yang, Y., 2010a. Crustal shear velocity structure of the western US inferred from ambient noise and earthquake data, *J. geophys. Res.,* **115,** B10306, doi:10.1029/2010JB007448.

Moschetti, M.P., Ritzwoller, M.H., Lin, F.C. & Yang, Y., 2010b. Seismic evidence for widespread western-US deep-crustal deformation caused by extension, *Nature,* **464,** 885–889.

Nakamura, Y., 1989. A method for dynamic characteristics estimation of subsurface using microtremor on the ground surface, *Q. Rep. Railw. Tech. Res. Inst.,* **30,** 25–30.

Nishida, K., 2013. Global propagation of body waves revealed by cross-correlation analysis of seismic hum, *Geophys. Res. Lett.,* **40**, 1691–1696.

Poli, P., Campillo, M., Pedersen, H. & the Lapnet Working Group, 2012. Body wave imaging of the Earth's mantle discontinuities from ambient seismic noise, *Science,* **338,** 1063–1065.

Pollitz, F.F. & Snoke, J.A., 2010. Rayleigh-wave phase-velocity maps and three dimensional shear velocity structure of the western US from local non-plane surface wave tomography, *Geophys. J. Int.,* **180,** 1153–1169.

Prieto, G.A., Denolle, M., Lawrence, J.F. & Beroza, G.C., 2011. On amplitude information carried by the ambient seismic field, *C. R. Geosci.,* **343,** 600–614.

Ritzwoller, M.H., Lin, F.C. & Shen, W., 2011. Ambient noise tomography with a large seismic array, *Compte Rendus Geosci*., **13,** doi:10.1016/j.crte.2011.03.007.

Sabra, K., Gersoft, P., Roux, P. & Kuperman, W., 2005. Extracting time-domain Green's function estimates from ambient seismic noise, *Geophys. Res. Lett.,* **32,** L03310, doi:10.1029/2004GL021862.

Saltus, R.W., 1993. Upper-crustal structure beneath the Columbia River Basalt Group, Washington: Gravity interpretation controlled by borehole and seismic studies, *Geol. Soc. Am. Bull.,* **105,** 1247–1259.

Sánchez-Sesma, F.J. *et al.*, 2011. A theory for microtremor H/V spectral ratio: application for a layered medium, *Geophys. J. Int.,* **186,** 221–225.

Savage, M.K., Lin, F.C. & Townend, J., 2013. Ambient noise cross-correlation observations of fundamental and higher-mode Rayleigh wave propagation governed by basement resonance, *Geophys. Res. Lett.,* **40,** doi:10.1002/grl.50678.

Schmandt, B. & Humphreys, E.D., 2011. Seismically imaged relict slab from the 55 Ma Siletzia accretion to the northwest United States, *Geology,* **39,** 175–178.

Shapiro, N.M., Campillo, M., Stehly, L. & Ritzwoller, M.H., 2005. High resolution surface wave tomography from ambient seismic noise, *Science,* **307,** 1615–1618.

Shen, W., Ritzwoller, M.H., Schulte-Pelkum, V. & Lin, F.-C., 2013a. Joint inversion of surface wave dispersion and receiver functions: a Bayesian Monte-Carlo approach, *Geophys. J. Int.,* **192,** 807–836.

Shen, W., Ritzwoller, M.H. & Schulte-Pelkum, V., 2013b, A 3-D model of the crust and uppermost mantle beneath the central and western US by joint inversion of receiver functions and surface wave dispersion, *J. geophys. Res.,* **118,** 1–15.

Snieder, R., 2004. Extracting the Green's function from the correlation of coda waves: a derivation based on stationary phase, *Phys. Rev. E,* **69,** doi:10.1103/PhysRevE.69.046610.

Tanimoto, T. & Rivera, L., 2008. The ZH ratio method for long-period seismic data: sensitivity kernels and observational techniques, *Geophys. J. Int.,* **172,** 187–198.

Tikoff, B. & Maxson, J., 2001. Lithospheric buckling of the Laramide foreland during Late Cretaceous and Paleogene, western United States, *Rocky Mountain Geology,* **36,** 13–35.

Trehu, A.M., Asudeh, I., Brocher, T.M., Luetgert, J.H., Mooney, W.D., Nabelek, J.L. & Nakamura, Y., 1994. Crustal architecture of the Cascadia forearc, *Science,* **266,** 237–243.

Tsai, V.C., 2011. Understanding the amplitudes of noise correlation measurements, *J. geophys. Res.,* **116,** B09311, doi:10.1029/2011JB008483.

Walker, J.D., Bowers, T.D., Glazner, A.F., Farmer, A.L. & Carlson, R.W., 2004. Creation of a North American volcanic and plutonic rock database (NAVDAT), *Geol. Soc. Am. Abstr. Programs,* **36**(4), 1–9.

Weaver, R.L., 2011. On the amplitudes of correlations and the inference of attenuations, specific intensities and site factors from ambient noise, *Compt. Rendus Geosci.,* **343,** 615–622.

Weaver, R.L., 2013. On the retrieval of attenuation and site amplifications from ambient noise on linear arrays: further numerical simulations, *Geophys. J. Int.,* **193,** 1644–1657.

Yang, Y., Ritzwoller, M.H. & Jones, C.H., 2011. Crustal structure determined from ambient noise tomography near the magmatic centers of the Coso region, southeastern California, *Geochem. Geophys. Geosyst.,* **12,** Q02 009, doi:10.1029/2010GC003362.

Yano, T., Tanimoto, T. & Rivera, L., 2009. The ZH ratio method for long-period seismic data: inversion for *S*-wave velocity structure, *Geophys. J. Int*., **179,** 413–424.

Yao, H., Van Der Hilst, R.D. & De Hoop, M.V., 2006. Surface-wave array tomography in SE Tibet from ambient seismic noise and two-station analysis—I. Phase velocity maps, *Geophys. J. Int.,* **166,** 732–744.

Yao, H., Beghein, C. & van der Hilst, R.D., 2008. Surface wave array tomography in SE Tibet from ambient seismic noise and two-station analysis—II. Crustal and upper-mantle structure, *Geophys. J. Int.,* **173,** 205–219.

Zhang, J. & Yang, X., 2013. Extracting surface wave attenuation from seismic noise using correlation of the coda of correlation, *J. geophys. Res.,* **118,** 2191–2205.